Characterizing facies, pore types, and diagenesis of a subtidal to peritidal carbonate platform for defining flow units

DOI:
10.2110/sepmsp.112.03

Document Version
Final published version

Published in:
Carbonate Pore Systems

CHARACTERIZING FACIES, PORE TYPES, AND DIAGENESIS OF A SUBTIDAL TO PERITIDAL CARBONATE PLATFORM FOR DEFINING FLOW UNITS

LUCY MANIFOLD, AHMED EL-BOZIE, CATHY HOLLIS, AND STEFAN SCHRÖDER
School of Earth and Environmental Sciences, Williamson Building, Oxford Road, University of Manchester, Manchester M13 9PL, UK
e-mail: lucy.manifold@manchester.ac.uk

ABSTRACT: Oil and gas reside in reservoirs within peritidal and shallow subtidal lagoonal carbonate sediments across the globe. This is a zone of facies heterogeneity, controlled by changes in depositional energy, water depth, clastic influx, and evapotranspiration. Close proximity to evaporitic brine pools means that it is also an environment with the potential for dolomitization during shallow burial. As a result, the original pore system of carbonate sediment can become drastically altered prior to burial, such that reservoir properties may not be predictable from facies models alone. The Miocene Santanyí Limestone Formation, Mallorca, Spain, is well exposed and has undergone minimal burial and therefore presents an excellent opportunity to integrate sedimentology, facies architecture, and diagenesis to determine how porosity evolves within individual facies in the shallow subsurface. From here, the impact on pore type, pore volume, pore connectivity, and petrophysical anisotropy can be assessed.

The Santanyí Limestone consists of pale mudstones and wackestones, rooted wacke-packstones, stratiform laminites, and skeletal and oolitic, cross-bedded grainstone. Thin-section analysis reveals a paragenetic pathway of grain micritization, followed by dissolution of aragonite, possibly by meteoric fluids associated with karstification. Subsequently, the unit underwent fracturing, compaction, recrystallization, cementation, dolomitization, and matrix dissolution to form vugs. Petrophysical analyses of 2.54-cm-diameter plugs indicate that these complex diagenetic pathways created petrophysical anisotropy [mean horizontal permeability (Kh)/vertical permeability (Kv) of whole formation = 3.4] and that measured parameters cannot be related directly to either geological facies or pore type. Instead, petrophysical data can be grouped according to the diagenetic pathways that were followed after deposition. The best reservoir quality (i.e., typical porosity 15 to >40% and permeability >100 mD) is associated with pale mudstones, stratiform laminites, and skeletal and oolitic grainstone that have undergone pervasive recrystallization or dolomitization. These rocks have the some of the lowest formation resistivity factor (FRF) values (<200) and thus the simplest pore system. The poorest reservoir properties (k <10 mD) occur in mudstones and wackestones that have not been recrystallized and, hence, are dominated by a simple network of micropores (FRF <101). Skeletal and oolitic grainstones and rooted and brecciated wacke-packstones that have undergone some cementation and partial recrystallization have moderate reservoir properties and a high FRF (>>1000), reflecting a complex pore system of biomolds, vugs, and microporosity. Consequently, reservoir properties can be predicted based on their primary rock properties and the diagenetic pathway that they followed after deposition.

KEY WORDS: Santanyí Limestone, petrophysics, peritidal, shallow-water platform, heterogeneity

INTRODUCTION

Carbonate strata deposited in peritidal and lagoonal environments can be important hydrocarbon reservoirs (e.g., Malampaya Platform, offshore Philippines [Fournier et al. 2004]; Natih Formation, Oman [Grélaud et al. 2010, Hollis et al. 2010]; Arab Formation, Arabian Gulf [Hollis et al. 2017, Marchionda et al. 2018]; Khuff Formation, Arabian Gulf [Adam et al. 2018]; Lekhwair Group, Oman [e.g., van Buchem et al. 2002, Strohmenger et al. 2006]). However, the presence of many depositional subenvironments influenced by autocyclic and allocyclic deposition can lead to complex facies architecture (e.g., James 1984), while diagenetic modification can result in a multitude of pore types and complex pore networks (e.g., Hollis 2011). Diagenetic overprint also means that facies-based reservoir models can be a poor guide to reservoir properties and performance. In order to capture these multivariant controls on reservoir properties, various workflows and methods have evolved within carbonate petroleum geology research (e.g., Lucia 2007, Ahr 2008, Hollis et al. 2010, Skalinski and Kenter 2015). A key factor used to constrain these rock-typing schemes, and predictively distribute them within interwell areas in models, is incorporation of the diagenetic pathways taken by individual sedimentary facies (e.g., Hollis et al. 2010, Skalinski and Kenter 2015).

Laterally continuous outcrops along the southeast coast of Mallorca (Balearic Islands, Spain) provide an excellent opportunity to describe depositional facies and early diagenesis of subtidal to peritidal environments in detail, and to understand depositional and diagenetic controls on reservoir heterogeneity (Pomar and Ward 1999). These rocks have undergone only minor tectonic tilting and have only experienced shallow burial of several tens of meters (Pomar and Ward 1999), thus preventing overprinting of shallow-burial diagenetic phases by deeper diagenetic events. This study examined the relationship between the sedimentological and diagenetic evolution of the Santanyí Limestone and its petrophysical rock properties (porosity, ϕ; permeability, k; capillary pressure, Pc; resistivity, Ro; and formation resistivity factor, FRF). The overall aim was to determine whether sedimentology or diagenesis has the most significant control on pore-type heterogeneity to aid predictability of flow properties in heterogeneous, peritidal limestone formations.

GEOLOGICAL SETTING

The Balearic Islands, including Mallorca, represent a prolongation of the Alpine Betic Chain of southern Spain (Gelabert et al. 1992), which was affected by Alpine orogenic movements during the Early Miocene (Burdigalian–Langhian) (Bernoulli and Jenkyns 1974). Thrusting of Triassic to Paleogene sedimentary rocks to the NW formed the present-day NE–SW-trending mountain ranges of the Sierra de Tramuntana and Sierra de Levante (Fig. 1A; Bizon et al. 1978; Alvaro et al. 1984; Gelabert et al. 1992). These are separated by a central depression bound by extensional faults where molasse sediments were deposited in the Late Miocene (Palma Basin; Gelabert et al. 1992). During tectonic quiescence in the Late Tortonian to Early

Carbonate Pore Systems: New Developments and Case Studies
DOI: 10.2110/sepmsp.112.03
SEPM Special Publication No. 112, Copyright © 2019
SEPM (Society for Sedimentary Geology), ISBN 978-1-56576-364-7, eISBN 978-1-56576-365-4, p. 108–125.

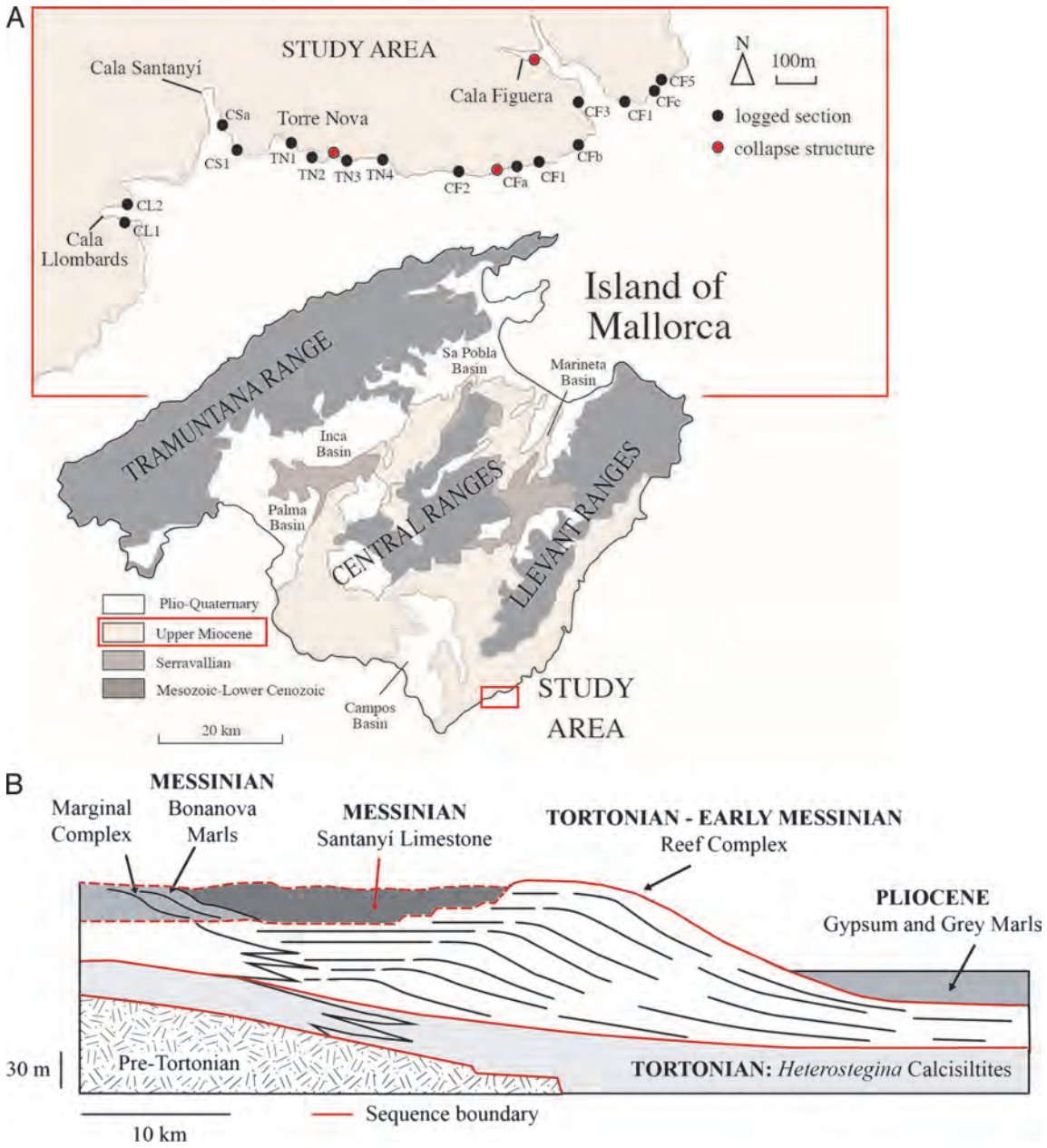

FIG. 1.—**A)** Simplified geological map of Mallorca with study area highlighted (modified from Sábat et al. 2011), and logged section localities in study area. **B)** Stratigraphic context of Santanyí Limestone with sequence boundaries, tentatively considered to be third-order sequences, after Pomar et al. (1996). More recently, the Santanyí Limestone was considered to be equivalent to the Reef Complex, represented by the dotted line (Arenas and Pomar 2010).

Messinian, land-attached carbonate platforms were established offshore of the emergent Sierra de Tramuntana and Sierra de Levante mountain ranges and extended for up to 20 km basinward (Pomar et al. 1996). Present-day thicknesses of individual carbonate platforms are approximately 100 m (Pomar et al. 1996).

The stratigraphy of the Tortonian–Messinian interval consists of three depositional packages that were tentatively considered as third-order sequences (Fig. 1B; Pomar 1991, Pomar et al. 1996): (1) the basal *Heterostegina* packstones with extensive rhodalgal biostromes, but no coral reefs (Early Tortonian); (2) the Late Tortonian–Early Messinian Reef Complex, with well-developed coral reef, fore-reef, shelf, and lagoonal facies; and (3) an upper sequence, generally assigned to the Messinian (6.3–5.2 Ma), but probably age-equivalent to the upper Reef Complex (Arenas and Pomar 2010), composed of grainstones, oolites and stromatolites (Santanyí Limestone, the subject of this study), evaporite, dolomite, and marls (Gypsum and Gray Marls), and fan delta conglomerates and marls (Bonanova Marls). Platform development was terminated at about 5 Ma by the major fall in relative sea level in the Messinian and subsequent evaporite deposition in the western Mediterranean (Pomar et al. 1996).

TABLE 1.—Summary table of sample names, locality of sample acquisition, lithology, and assigned facies name.

Sample name	Grid reference (WGS84)	Lithology	Facies
TN1	0513175, 4353150	Limestone	Brecciated mudstone with marl
TN2	0513175, 4353151	Limestone	Moldic wacke-mudstone
TN3	0513275, 4353050	Limestone	Oyster rudstone
TN4	0513275, 4353051	Limestone	Rooted wacke-packstone
TN5	0513325, 4353120	Limestone	Pale mudstone
TN6	0513325, 4353121	Limestone	Moldic wacke-mudstone
TN7	0513325, 4353122	Limestone	Rooted wacke-packstone
TN8	0513325, 4353123	Limestone	Rooted wacke-packstone
TN9	0513675, 4353050	Limestone	Moldic wacke-mudstone
TN10	0513675, 4353051	Limestone	Rooted wacke-packstone
CF1	0514737, 4353065	Limestone	Moldic wacke-mudstone
CF2	0514737, 4353066	Limestone	Skeletal accumulations
CF3	0514737, 4353067	Limestone	Skeletal accumulations
CF4	0514200, 4352950	Limestone	Moldic wacke-mudstone
CF5	0514825, 4353120	Dolostone	Pale mudstone
CF6	0514825, 4353121	Limestone	Rooted wacke-packstone (layered)
CF7	0515130, 4353350	Limestone	Rooted wacke-packstone
CF8	0515375, 4353420	Limestone	Brecciated and rubbly wacke-packstone
CF9	0515375, 4353421	Limestone (recrystallized)	Stratiform laminites
CS1	0152797, 4353176	Limestone/dolostone	Oyster rudstone
CS2	0152797, 4353177	Limestone/dolostone	Oyster rudstone
CS3	0152797, 4353178	Limestone	Brecciated and rubbly wacke-packstone
CS4	0152797, 4353179	Dolostone	Stratiform laminites
CL1	0512170, 4352800	Limestone	Aligned moldic wacke-mudstone
CL2	0512170, 4352801	Limestone/dolostone	Aligned moldic wacke-mudstone
CL3	0512200, 4352740	Limestone	Rooted wacke-packstone

WGS84 = World Geodetic System 1984.

METHODS

Field mapping, logging, and sampling took place at the Cala Figuera, Cala Santanyí, Sa Torre Nova, and Cala Llombards localities along a 2-km transect of the Santanyí Limestone Formation on the southeast coast of Mallorca (Fig. 1A). The transect is approximately parallel to strike, with the inferred platform margin located a few kilometers to the SE (Robledo Ardila et al. 2004). Rock samples were taken from each logged locality (27 total; Table 1) and named according to their geographical locality. Sampling captured all sedimentary facies (e.g., grain type, color, pore type). Skeletal and oolitic grainstone, and coral rudstone were undersampled due to their locations on high cliff faces (grainstone) and beneath the accessible outcrop (rudstone). Spatially restricted facies (oyster rudstone, aligned moldic wacke-mudstone) are also represented by only few samples.

From each sample, plugs were drilled in two orientations, one perpendicular and one parallel to bedding, using a stainless-steel rock corer with a 2.54-cm-wide diamond drill bit, providing a sample set of 43 core plugs (20 vertical, 23 horizontal). The potential of plug fracturing was reduced by using water, circulated by a pump, as well as by lowering the drill bit slowly into the sample. Plug ends were sliced using a trim saw for thin-section preparation. Plug ends were sanded using a diamond sanding disc and 240-grit wet and dry sanding paper to ensure a completely flat surface. For identification of carbonate minerals, thin sections were half-stained with an alizarine-red S^{+} potassium ferrocyanide solution. Grains, cements, micrite (defined as microcrystalline calcite), and pore types were quantified using point-counting software Petrog (200 points per sample). Pore types were identified using the porosity classification scheme of Choquette and Pray (1970).

Once plugged and trimmed, samples were dried in an oven set to 60° C. Samples were periodically weighed using an electronic balance (uncertainty ± 0.0005) to determine the rate at which water was lost (<0.02 ml/hr). While weighing the samples, care was taken not to abrade the surface and loosen material to preserve accuracy of measurements. Samples required 240 hours of drying before becoming fully dehydrated for petrophysical measurements.

Dried plugs up to 12 cm in length were measured using digital calipers (uncertainty ± 0.005) in eight directions, and the bulk volume (Vb) was calculated. The plug diameter was measured in numerous directions due to slight diversion of the tool during coring. Helium was intruded into the sample at a confining pressure of 18 bar using a ResLab© Helium gas porosimeter, and grain volume (Vg) was measured, from which the pore volume (Vp) was calculated ($Vp = Vb - Vg$). Samples with macroscale uncemented fractures that split under pressure during measurement were discarded. Fractures in facies D_1 were partially cemented, and thus these samples were preserved. Plugs were then placed into a Hassler cell, and permeability was determined using nitrogen intrusion within a ResLab DGP-200 Digital Gas Permeameter with an upper limit of 10,000 mD. Samples were analyzed three times each in the porosimeter and permeameter, and an average value was calculated. Porosity and permeability were plotted against each other, and trends were identified using the least squares methods. Microporosity, both intraparticle and intercrystalline, was calculated by subtracting all visible pore space in thin sections (macroporosity, defined by point counting) from total (helium) porosity (microporosity = helium porosity − modal porosity).

Once porosity and permeability measurements were complete, resistivity was determined on a subset of seven plugs, chosen to represent a range of the most common lithofacies over the lateral distance across the study area. Plugs were saturated with a 2% KCl brine by weight under vacuum for 24 hours. The conductivity of the brine was measured using a Bibby SMC1 meter with a Bibby SMC/08 electrode, converted to resistivity, and then normalized to 25° C using Arp's equation: Rw (25° C) = Rw ([T_1 + 21.5]/[46.5]), where T_1 is the ambient temperature at the time of measurement. The resistivity of the core plugs (Ro) was then measured using a CoreLab ARS-250 ambient resistivity core holder in combination with a FLUKE PM6306 RCL Resistance-Capacitance-Inductance meter. Two point measurements were made at 300-Hz frequency by placing the plug between two brine-soaked filter papers and two electrodes.

The dry plugs and brine-saturated plugs were weighed, and the density of the 2% KCl brine was measured. Capillary pressure was determined by desaturation of the brine-saturated samples using a Core Labs^{TM} Capillary Pressure Desaturation Cell System CPP-300, which contains a porous plate desaturation cell. Pressure was increased in increments of 0.4 bar to a maximum of 4.9 bar, close to the maximum threshold of the 5-bar porous plate. The FRF was calculated as the ratio of the resistivity of the brine-saturated plug (Ro) to the brine resistivity (Rw); i.e., FRF = Ro/Rw. Pore-throat radii were calculated from capillary pressure data using the formula $ri = (2\sigma \times \cos\theta \times 145.1 \times 10^{-3})/Pc$, where ri = pore-throat radius, σ = interfacial tension (72 dynes/cm), θ = contact angle (26.2°), and Pc = capillary pressure.

Mineralogy of marl samples was investigated using X-ray diffraction at the Williamson Research Centre of the University of Manchester using a Bruker D8 Advance Diffractometer (Cu Kα X-ray source). Samples were scanned from 5 to 70° 2θ using a step size of 0.02° and a counting time of 0.2 seconds per step.

DEPOSITIONAL FRAMEWORK OF THE SANTANYÍ LIMESTONE

Within the study area, the Santanyí Limestone shows a uniform vertical succession of seven main facies. An additional six facies are locally developed (Table 2). The type section (Fig. 2) and its interpreted depositional evolution are discussed below.

Vertical Facies Succession

The facies form discreet layers that can be walked out along a lateral coastal transect of 2 km (Fig. 3). The base of the Santanyí Limestone occurs in all sections as an erosional surface on top of coral framestones belonging to the Reef Complex. Draping the surface, there is a <4.5-m-thick coral rudstone (A; Table 2) with a diverse faunal assemblage of corals, bivalves, coralline algae, miliolid foraminifera, gastropods, bryozoa, serpulids, peloids, and coated grains. Most grains are fragmented. Sharply overlying the rudstone, there are 1 to 2 m of skeletal wacke-mudstones with scattered gastropods and thin-shelled bivalves, as well as rare bryozoa, miliolid foraminifera, and fragmented dasycladacean and coralline algae (B_1). At the top of B_1, there are occasional isolated breccia packages up to 30 cm thick, laterally equivalent to the marl (H_1) comprising partially cemented crackle breccia (sensu Morrow 1982), which contains heavily fragmented shell hash between clasts.

Overlying facies B_1, skeletal components become more abundant (skeletal wackestone) and occur mostly as millimeter-scale molds (C_1; 1–2 m thick). Molds are of whole bivalves and gastropods and often increase in abundance to the top of individual beds. Oyster fragments, fragmented corals, miliolids, rare ostracods, peloids, and ooids also occur. This limestone locally contains centimeter-scale vertical pipes cemented by calcite. Aligned moldic wacke-mudstone (C_2) is a related subfacies, where 50% of skeletal allochems are aligned horizontally.

A distinct 1- to 3-m-thick unit of skeletal grainstones and packstones dominated by miliolids, thin-shelled bivalves, coralline algae, rare ostracods, and fecal pellets (D_1, D_2) overlies facies C_1 and C_2. From the base upward, it comprises matrix-supported rubble pack breccia (sensu Morrow 1982) and then nodular fabrics (D_1) before being cut by vertical pipes (D_2) up to 30 cm in height. This measurement is important to consider during analysis because this fabric is below the representative element volume. Breccia clasts are subrounded, up to 0.5 to 9 cm in diameter, often normally graded, and supported by a noncemented carbonate mud matrix. When D_1 beds are thin, D_2 beds typically are thick (Fig. 3). The basal brecciated subfacies thins to the SW of the study area, in parallel with a reduced degree of brecciation and more rounded clasts. Overlying skeletal packstone with nodular and pipe fabrics (D_2) concurrently thickens to the SW. Nodules are subrounded and 2 to 5 cm in diameter. They are often aligned vertically and decrease in diameter up section. Cemented, subvertical pipes (length <35 cm, diameter <8 cm) extend to the bed top and may have a white, dusty surrounding matrix, or they may be cemented. Fragmented corals, 5 to 20 cm in size, are scattered throughout. Red micritic crusts (millimeter thick) occur repeatedly within this facies and define bedding surfaces.

Overlying the piped and nodular facies, there is a gradation up section to a 2- to 6-m-thick unit of stratiform crinkly laminites (E_2). Individual laminations are between 0.5 and 5 mm thick and relatively smooth, and they form centimeter-scale domes, with red micritic crusts commonly interbedded. Laminae can be traced laterally over several meters and alternate with crystalline carbonates, skeletal and oolitic grainstones, or locally shelly coquinas similar to skeletal rudstone. Allochems include molds of bivalve fragments, as well as coralline algae, miliolids, peloids, and ooids.

The top of the Santanyí Limestone is formed by a <20-m-thick cliff of skeletal and oolitic grainstone with horizontal lamination, symmetrical and asymmetrical ripple lamination, trough cross-lamination, and locally herringbone cross-lamination (F_1). The scale of cross-lamination varies from 2 to 5 cm for herringbone cross-lamination to 10 cm for trough cross-lamination. Discrete beds are intensely bioturbated with *Planolites* burrows (F_2). These cylindrical tubes are 1 cm in diameter and subparallel to bedding. Where the tubes are present, physical sedimentary structures are strongly masked or absent. The microfacies consists of crystalline calcite with abundant millimetric and centimetric molds of nonskeletal and skeletal grains. Locally, peloids and textulariid foraminifera are preserved.

Associated Facies

Oyster rudstones (B_2) occur locally with a maximum thickness of 70 cm and lateral extent of 15 m. They are associated with mudstones (B_1) and moldic wacke-mudstones (C_1), and they have undulating erosive basal contacts. Whole oysters up to 10 cm in size make up at least 20% of the facies and locally form decimetric high-abundance pockets 1 to 4 m apart. In addition to oysters, other fragmented bivalves, encrusting serpulids, solitary and colonial corals (*Porites astreoides*), fragmented miliolids, peloids, and ooids were observed.

Locally, decimeter-thick stratabound skeletal rudstone with erosive basal contacts, forming a weakly cemented coquina-type deposit (D_3), is present as decimetric wedge-shaped packages. It lacks a matrix and thins over a lateral distance of 30 cm in both directions. Such skeletal rudstone increases in abundance to the SW of the study transect.

Below stratiform laminites, thin-bedded peloidal skeletal packstone with irregular-nodular bedding occurs in the western part of the field area. The most characteristic features are several centimeter-

TABLE 2.—Summary of facies composition, grain size range, porosity, permeability, pore types, and diagenesis.

Facies	Skeletal allochems (listed in decreasing abundance)	Nonskeletal allochems (listed in decreasing abundance)	Grain size range
Coral rudstone (A)	Coral (0.5–4 mm) Bivalves (0.2–2 mm) Coralline algae (0.5–1.5 mm) Miliolids (0.25 mm) Gastropods (molds) Bryozoa (0.5 mm) Serpulid worm tube (<0.5 mm) Echinoderm (0.4 mm)	Peloids (0.1 mm) Grapestone intraclasts (0.3 mm)	0.1–3.5 mm $\bar{x} = 0.2$ mm
Pale mudstone (B_1)	Miliolids (0.6 mm) Gastropods (<2 mm) Bivalves (geopetal) (0.5 mm) Bryozoa (0.9 mm) Coral (5 mm) Dasycladacean algae Coralline algae	Peloids, elongate (0.01 mm)	0.01–5 mm $\bar{x} = 0.05$ mm
Oyster rudstone (B_2)	Bivalves/oysters (0.6 mm) Serpulid worm tubes (<0.8 mm) Bryozoa (0.8 mm) Solitary coral (0.6 mm) Miliolids (0.2 mm) Colonial corals (*Porites astreoides*) (dm)	Peloids (0.2 mm) Ooids (0.2 mm)	0.01–1.5 mm $\bar{x} = 0.2$ mm
Moldic wacke-mudstone (C_1) and aligned moldic wacke-mudstone (C_2)	Gastropods (2 mm) Bivalves (0.8–2 mm) Miliolids (0.1 mm) Coralline algae, fragmented (0.1 mm)	Peloids, elongate (0.1–0.7 mm) Ooids (0.1–0.7 mm)	0.1–2 mm $\bar{x} = 0.2$ mm
Brecciated and rubbly wacke-packstone (D_1)	Miliolids (0.05–0.45 mm) Bivalves (0.4 mm)	Peloids (0.1 mm)	0.01–0.45 mm $\bar{x} = 0.06$ mm
Rooted wacke-packstone (D_2)	Miliolids (0.1–0.4 mm) Gastropods (0.2 mm) Bivalves (0.2 mm) Ostracods (0.2 mm)	Peloids (0.2 mm) Ooids (0.2 mm)	0.01–3 mm $\bar{x}$ = variable
Skeletal rudstone (D_3)	Gastropods (<1 mm) Miliolids (0.2 mm) Fragmented coralline algae, tubular plant, solitary coral	Peloids (0.1–0.5 mm) Ooids (0.3–0.5 mm)	0.01–12 mm $\bar{x} = 0.4$ mm
Cyclocardium packstone (E_1) and stratiform laminites (E_2)	Bivalves (1–2 mm) Miliolids (0.2 mm) Coralline algae (0.5 mm)	Peloids (0.05–0.4 mm) Ooids (0.1–0.8 mm)	0.01–0.6 mm $\bar{x} = 0.4$ mm
Skeletal and oolitic grainstone (F_1, F_2) and mounded laminites (G_1, G_2)	Mostly destroyed by diagenesis Textulariid foraminifera (0.2–0.8 mm)	Mostly destroyed by diagenesis Peloids (0.05–0.4 mm)	0.05–15 mm (molds)

thick shell beds consisting of *Cyclocardium* sp. bivalves (E_1) (Coppes 2007). Bivalves tend to occur as molds with both shells together and convex up. The microfacies is dominated by fecal pellets and bivalves. Red micritic crusts are developed in the upper part (Coppes 2007). There is a gradational contact with stratiform laminites.

Grainstones (F_1 and F_2) are closely associated with two types of mounded laminites (microbialites; Arenas and Pomar 2010): (1)

TABLE 2.—*Extended*.

Depositional setting	Porosity (ϕ), microporosity ($\mu\phi$), and permeability (k)	Pore types	Diagenesis
Back-reef, washover	No data	Moldic Interparticle	Mechanical compaction Aragonite dissolution Micritization Isopachous microsparite
Low-energy, subtidal lagoon	$\bar{x}\phi = 14.2\%$ (10.5–28.6%) $\mu\phi = 6.6\%$ (4.6–8.5%) $\bar{x}k = 704$ mD (6.4–1781 mD)	Fracture Moldic Vuggy Channel	Aragonite dissolution Micritization Minor fracturing Cementation Fabric-destructive (FD) dolomitization
Patch reef	$\bar{x}\phi = 13.7\%$ (7.6–23.1%) $\mu\phi = 0\%$ $\bar{x}k = 10.2$ mD (7.5–11.2 mD)	Moldic Fracture	Micrite envelopes Isopachous microsparite cementation Fabric-retentive (FR) dolomitization
Back-lagoon, peritidal	$\bar{x}\phi = 20.1\%$ ($C_1 = 7.0$–34.0%) ($C_2 = 15.2$–16.0%) $\mu\phi = 13.5\%$ (3.5–25.8%) $\bar{x}k = 13.6$ mD ($C_1 = 5.5$–193 mD) ($C_2 = 1923$–3721)	Moldic Intraparticle Fracture	Aragonite dissolution Micritization Minor fracturing Cementation FR dolomitization
Emergent, calcrete	$\bar{x}\phi = 13.1\%$ (6.9–17.4%) $\mu\phi = 6.9$ (2.9–11.9) $\bar{x}k = 62.8$ mD (7.8–487 mD)	Moldic Vuggy Interparticle	Aragonite dissolution Micritization Cementation
Intertidal, mangrove swamp	$\bar{x}\phi = 11.7\%$ (6.0–36.8%) $\mu\phi = 5.0$ (0.8–10.4) $\bar{x}k = 6.4$–16.8 mD (6.4–26.1 mD)	Interparticle Moldic Vuggy Channel	Aragonite dissolution Micritization Minor fracturing Cementation
Coquina	$\bar{x}\phi = 38.4\%$ (36.0–41.1%) $\mu\phi = 3\%$ $\bar{x}k = 695$ mD (223–1166 mD)	Moldic Vuggy Interparticle	Aragonite dissolution Micritization Cementation
Intertidal	$\bar{x}\phi = 29.4\%$ (28.0–30.7%) E_1 $\mu\phi = 6.5$ (4.6–8.5) $\bar{x}k = 2196$ mD (12.8–5676 mD)	Interparticle Intercrystalline Moldic Vuggy Fenestral	Aragonite dissolution Micritization FD and FR matrix neomorphism (calcite)
Tidal sandbar	$\bar{x}\phi = 21.6\%$ (8.24–39.15%) $\bar{x}k = 267.6$ mD (<1–535.37 mD)	Intercrystalline Biomoldic	FD matrix neomorphism (calcite)

Horizontal micritic laminae form millimeter-scale crinkly laminations and locally centimeter-high domes and columns (G_1). Laminations grade laterally and vertically over less than 1 m into F_1 and F_2 (Arenas and Pomar 2010). Micritic microbial laminae locally stabilize the ripples. (2) Centimeter- to meter-scale stromatolitic and thrombolitic bioherms (G_2) also occur. The largest bioherms reach 1 to 5 m and consist of thrombolitic (clotted) cores and laminated (stromatolitic) peripheries (Arenas and Pomar 2010).

Centimeter- to decimeter-thick blue-gray marls are interbedded in the limestone succession (H_1). The most prominent marl occurs at the

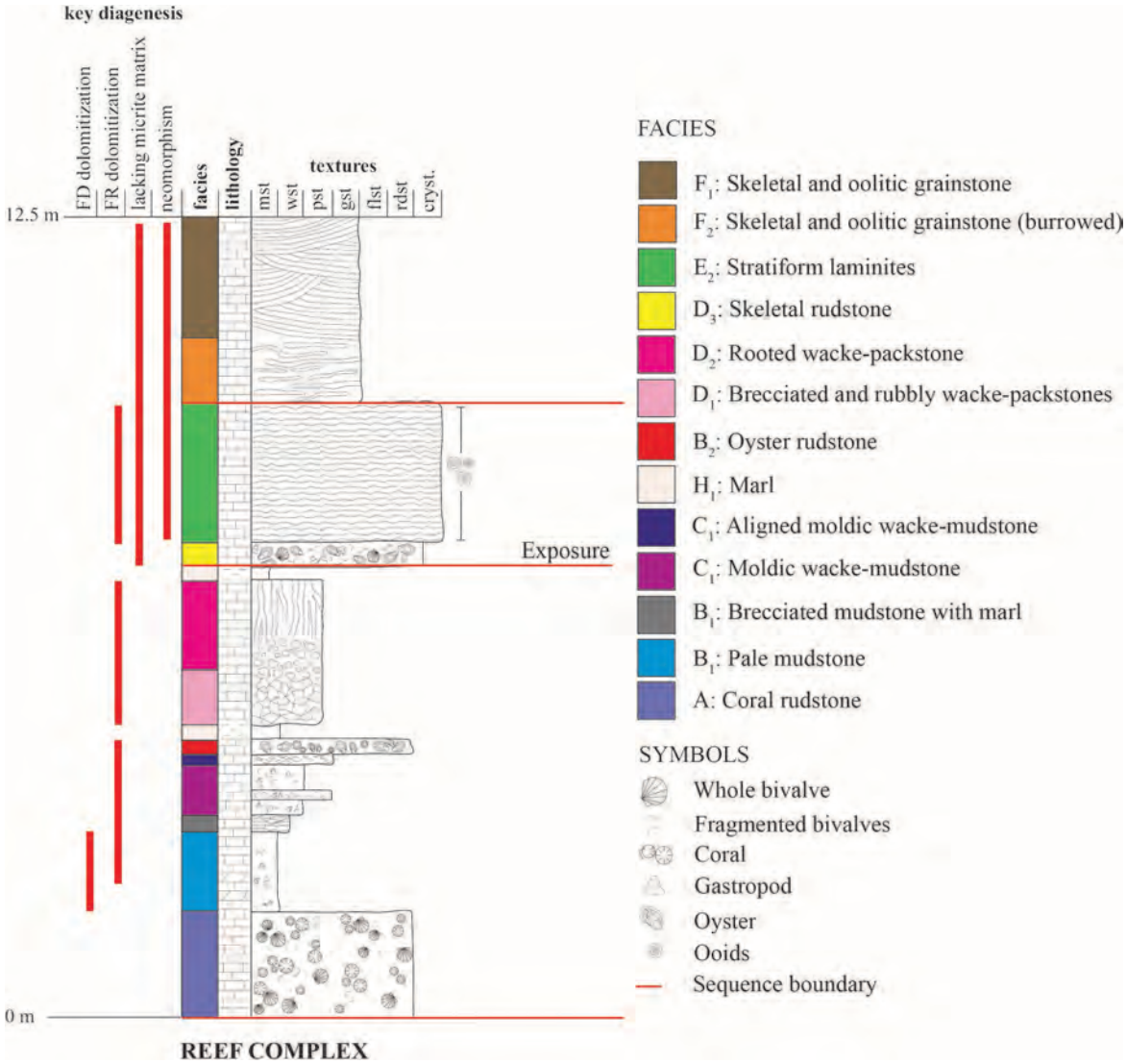

FIG. 2.—Ideal section demonstrating the vertical succession of facies above the Reef Complex and distribution of main pore-generating diagenetic processes. Note: FR = fabric retentive; FD = fabric destructive.

top of the rooted-nodular packstones (D_2) and between mudstones (B_1) and moldic wacke-mudstone (C_1). It contains black pebbles at its base. X-ray diffraction analysis identified quartz, calcite, montmorillonite, and muscovite.

Diagenesis

The following diagenetic products dominate within the Santanyí Limestone (Figs. 4, 5):

- Micrite envelopes preferentially occur on miliolid foraminifera and algal-coated grains (ooids; red arrow, Fig. 4A) and commonly also coat bivalve fragments. Some smaller bioclasts have been wholly micritized and are thus difficult to identify (blue arrow, Fig. 4A).
- Whole-rock recrystallization by calcite occurs in facies E_2, F_1, F_2, G_1, and G_2. Recrystallization is mimetic in stratiform laminites, preserving the original laminations (black arrows, Fig. 4B). Partial, finely crystalline, mimetic recrystallization by calcite is common, and calcite may also be replacive of skeletal tests in facies E_2.
- Most limestone facies have undergone calcite cementation in the form of drusy sparite, which binds grains and infills approximately half of microfactures and matrix pores (black arrows, Fig. 4C). Coarsely crystalline, sparry cements show a bladed habit, growing inwards into open pore space.
- The Santanyí Limestone is partially dolomitized throughout, giving a brown color in outcrop. Dolomitization is not facies selective, although it is more common towards the top of the succession. Up to 10% of samples contained dolomite when observed in thin section. Partial, fabric-retentive dolomitization occurs in moldic wacke-mudstone facies, oyster rudstone, and stratiform laminites (black arrows, Fig. 4F). Finely crystalline, fabric-destructive stratabound dolomite is restricted to the pale mudstone facies (B_1) when it is located beneath the brecciated mudstone/marl facies (Fig. 4E).

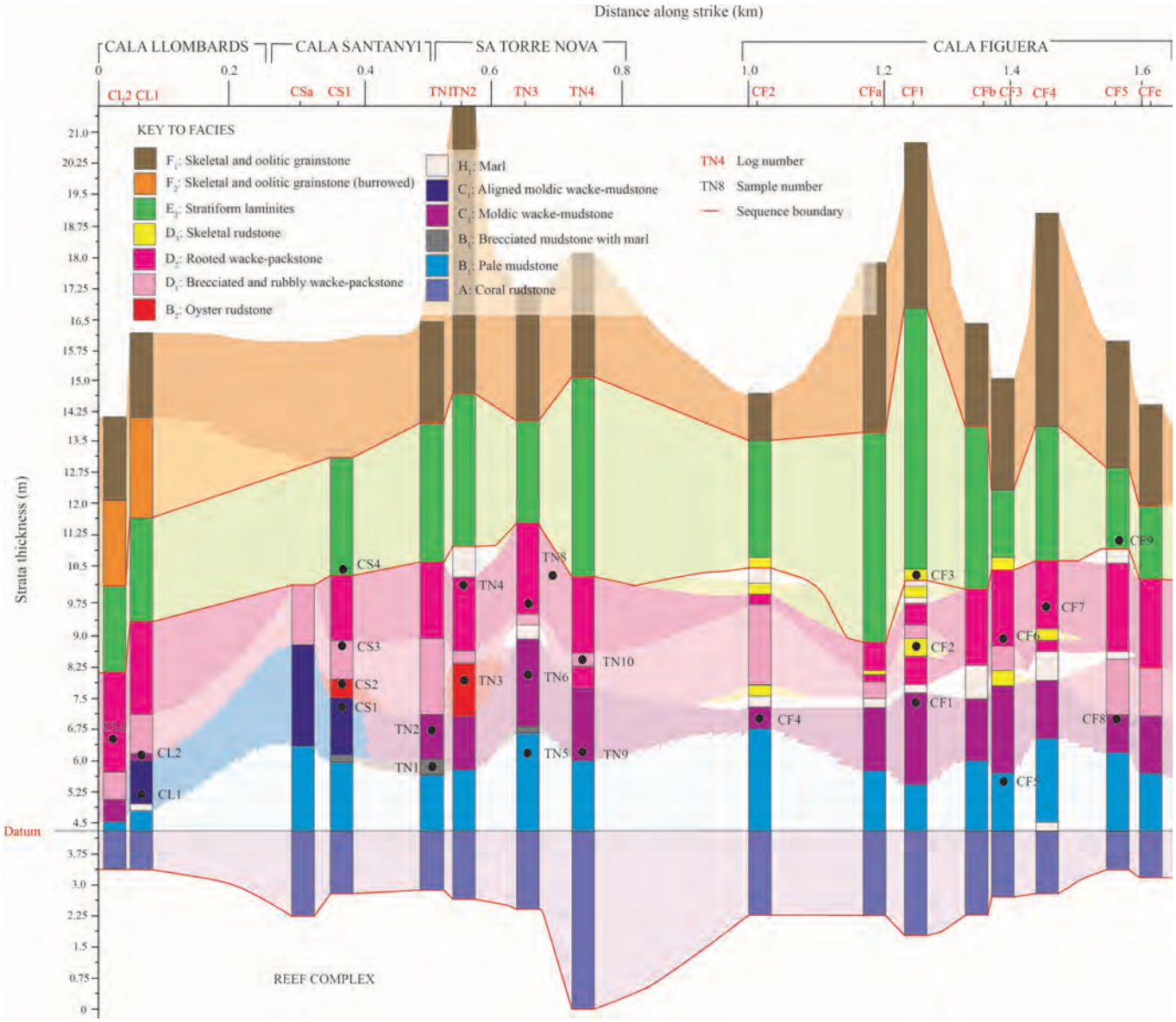

FIG. 3.—Correlation of lithofacies across the study area, with sequence boundaries. Datum is the top of the back-reef rudstone, due to the lateral traceability of this unit.

- Brittle fragmentation of micritized grains, intrapenetration of grains by pressure solution, and microfracturing are observed in thin section, but no stylolitization was observed in the field or on a microscopic scale.

Pore Types

Pore types were described from thin sections using transmitted light microscopy. Primary interparticle porosity is not preserved within the Santanyí Formation, and hence porosity is entirely secondary in origin. It forms by the following processes:

- Skeletal grains, principally bivalves and gastropods, dissolve to form biomolds (black arrows; Fig. 4A), which are evident in every sample in varying abundance, but particularly in wacke-mudstones (B_1, C_1, C_2) and rooted and brecciated wacke-packstones (D_2). Although moldic pores appear isolated in thin section, it is possible that they are connected via matrix micropore throats.
- Recrystallization (dolomitization or recrystallization by calcite) forms intercrystalline porosity.
- Vugs, up to 5 mm ($\bar{x} = 1$ mm) in diameter, occur throughout the whole formation but are smaller and less abundant in mudstone and wackestone facies. Vugs are enhanced by recrystallization and form the highest porosity.

Petrophysics Results

Porosity in the Santanyí Formation is good ($\phi = 4.6$–41.1%, ($\bar{x}\phi = 17.0\%$), with calculated microporosity up to 25.8% (C_1) (mean $\phi/\mu\phi$

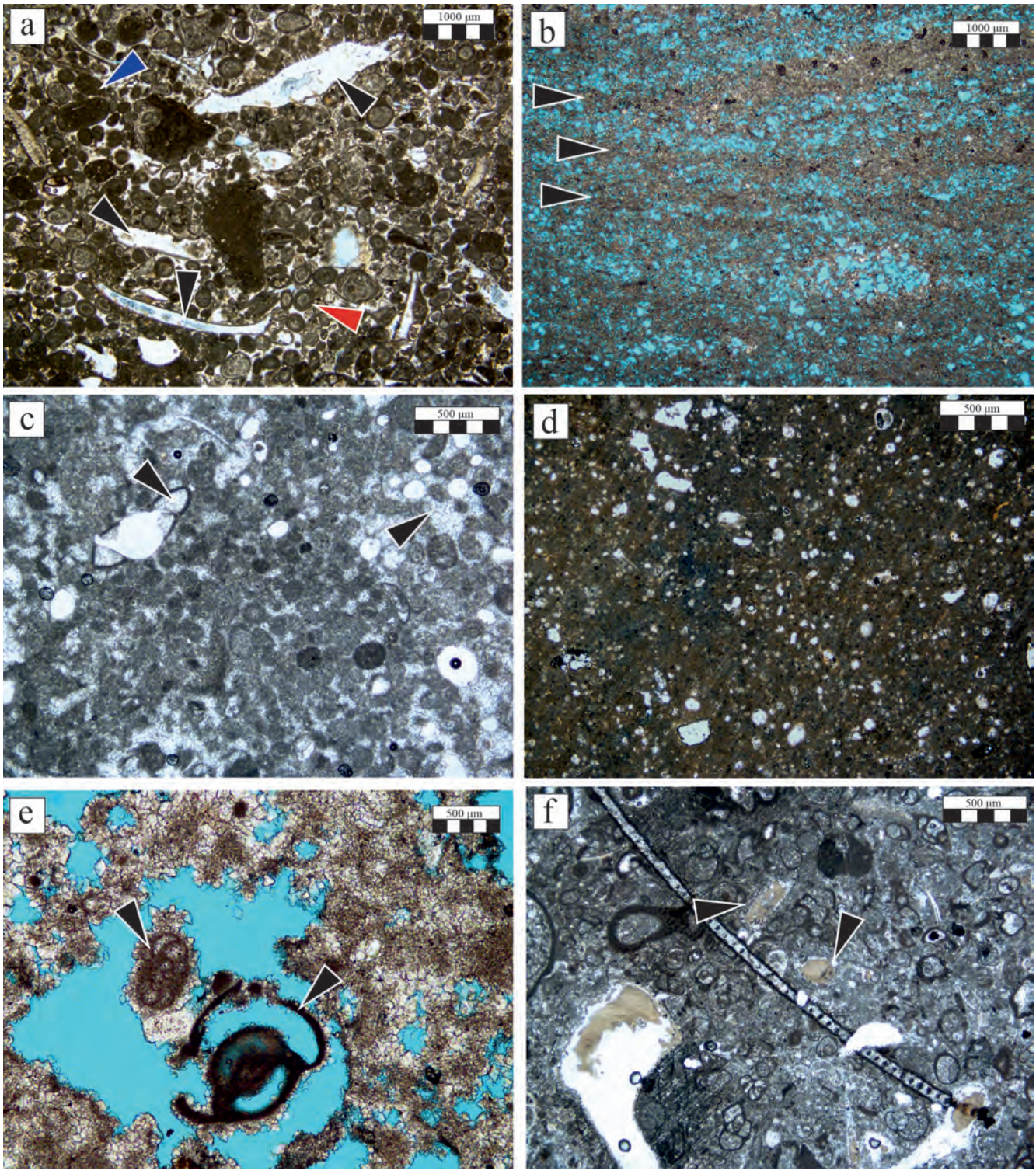

FIG. 4.—**A)** CS4 (E_2): poorly connected moldic porosity in an ooidal pack-grainstone (black arrows) with micritized ooids (red arrow) and wholly micritized grains (blue arrow). $\phi v = 30.7\%$; $\phi h = 29.1\%$; $kv = 12.8$ mD; $kh = 16.2$ mD. **B)** CF9 (E_2): recrystallized matrix of stratiform laminites with horizontally aligned moldic and intercrystalline pores (black arrows). $\phi v = 28.0\%$; $\phi h = 29.9\%$; $kv = 5677$ mD; $kh = 3075$ mD. **C)** CL3 (D_2): cemented intergranular (peloids and forams) and moldic porosity (black arrows). $\phi h = 12.9\%$; $kh = 9.2$ mD. **D)** CF4 (C_1): high volume of poorly connected small pores. $\phi v = 36.8\%$; $\phi h = 32.0$–34.8%; $kv = 1.3$; $kh = 14.0$–14.6 mD; $R_o = 11$; FRF = 32. **E)** CF5 (B_1): dolomitized pale mudstone with micritized miliolid (black arrow). $\phi v = 20.4\%$; $\phi h = 17.6\%$; $kv = 323.0$ mD; $kh = 1781.8$ mD; $R_o = 55$; FRF = 163. **F)** CF9 (E_2): partially dolomitized (black arrows) foraminiferal packstone. $\phi v = 28\%$; $\phi h = 29.9\%$; $kv = 5676.6$ mD; $kh = 3075.1$ mD.

TABLE 3.—Summary of all physical data, including petrophysical anisotropy. A dash indicates no data. Where there is an average value, multiple thin sections were analyzed.

Sample	Facies	Porosity (%)	Average (%)	Anisotropy (%)	Permeability (mD)	Average (mD)	Anisotropy (mD)	Bulk density (g/cm^3)	Grain density (g/cm^3)	Dolomite (%)	Authigenic calcite (%)	Micrite (%)	Resistivity (Ω·m)	FRF
CF8v	D_1	10.0	13.7	7.4	39.0	263.0	448.17	2.4	2.68	—	—	—	—	—
CF8h		17.4			487.1			2.2	2.66	0.0	4.25	58.0	—	—
CS3v	D_1	10.2	10.2	0.7	16.5	15.5	1.99	2.4	2.64	—	—	—	—	—
CS3h		10.9			14.5			2.3	2.62	0.0	65.0	0.0	—	—
TN4v	D_2	14.6	13.9	1.8	26.1	23.7	4.88	2.3	2.68	—	—	—	55	163
TN4h		12.9			21.3			2.3	2.68	0.0	81.5	0.0	—	—
CF9v	E_2	28.0	29.0	1.9	5676.6	4375.8	2601.52	1.8	2.78	—	—	—	—	—
CF9h		29.9			3075.1			1.9	2.77	70.5	0.0	0.0	—	—
TN7v	D_2	7.7	7.3	0.8	7.8	25.5	35.42	2.1	2.61	—	—	—	—	—
TN7h		6.9			43.2			2.4	2.43	0.0	$\bar{x} = 22.5$	$\bar{x} = 36$	—	—
TN2v	C_1	12.1	14.2	4.4	13.6	17.4	7.57	2.2	2.62	—	—	—	—	—
TN2h		16.4			21.2			2.2	2.56	0.0	10.0	14.5	—	—
CF2v	D_3	41.1	38.5	5.1	1166.1	117.9	943.06	1.6	2.56	0.0	—	—	—	—
CF2h		36.0			223.0			1.7	2.67	0.0	7.0	31.5	—	—
CS4v	E_2	30.7	29.9	1.6	12.8	15.8	5.94	1.8	2.61	—	—	—	—	—
CS4h		29.1			16.2			1.9	2.63	0.8	21.5	10.0	34	101
CF1v	C_1	18.0	17.1	1.7	18.8	14.8	7.89	1.8	2.67	—	—	—	—	—
CF1h		16.3			10.9			1.7	2.67	—	—	—	—	—
CL2v	C_2	24.0	17.2	13.0	13.8	11.6	7.64	2.0	2.68	—	—	—	—	—
CL2ha		13.6			6.6			2.3	2.60	0.5	34.0	42.5	60	180
CL2hb		16.5			14.3			2.2	2.63	—	—	—	—	—
TN9v	C_1	7.0	11.5	9.0	5.5	11.1	11.03	2.5	2.70	—	—	—	527	1566
TN9h		16.0			16.6			2.2	2.66	0.0	25.5	—	—	—
CF6v	D_2	13.4	14.7	2.6	14.4	23.8	17.11	2.3	2.69	—	—	—	—	—
CF6ha		14.6			23.3			2.3	2.70	—	—	—	—	—
CF6hb		16.0			33.7			2.3	2.69	—	—	—	—	—
CS1v	B_2	7.6	n/a	n/a	7.5	n/a	n/a	2.5	2.67	0.0	23.5	42.5	—	—
TN5h	B_1	4.6	n/a	n/a	6.5	n/a	n/a	2.6	2.65	0.5	35.0	17.0	—	—
TN3v	B_2	23.1	16.8	12.6	11.2	11.6	0.7	1.9	2.58	—	—	—	—	—
TN3h		10.5			11.9			2.3	2.57	0.0	17.0	32.5	—	—
TN1v	B_1	28.6	n/a	n/a	73.7	n/a	n/a	1.9	2.67	0.0	3.5	52.0	—	—
TN10v	D_2	6.0	n/a	n/a	6.4	n/a	n/a	2.5	2.73	0.0	3.5	93.0	—	—
CL1v	C_2	16.0	15.6	0.8	192.7	1956.9	3528.5	2.2	2.67	—	—	—	—	—
CL1h		15.2			3721.2			2.2	2.66	0.0	0.0	82.0	—	—
TN8v	D_2	11.7	13.5	3.5	10.7	10.5	0.28	2.3	2.60	—	—	—	1750	5206
TN8h		15.3			10.4			2.2	2.61	—	—	—	—	—
CF5v	B_1	20.4	19.0	2.9	323.0	1052.4	1458.79	2.1	2.71	—	—	—	—	—
CF5h		17.6			1781.8			2.2	2.71	0.0	55.0	46.5	55	163
CF4v	C_1	36.8	34.6	4.8	13.3	13.9	1.3	1.7	2.77	—	—	—	11	32
CF4ha		34.8			14.0			1.8	2.76	0.0	0.0	82.5	—	—
CF4hb		32.0			14.6			1.9	2.75	—	—	—	—	—
CL3h	D_2	12.9	n/a	n/a	9.1	n/a	n/a	2.2	2.52	0.0	34.0	2.5	—	—
CF7h	D_2	16.4	n/a	n/a	21.0	n/a	n/a	1.8	2.63	0.0	32.5	6.5	—	—

= 3.1). Permeability is variable, ranging between <0.01 mD and 4236 mD ($\bar{x}k$ = 400 mD). Averages and ranges of porosity and permeability, as well as pore-type diagenetic processes associated with each facies, are summarized in Table 2. There is no correlation between porosity and permeability and little evidence for a textural control (Dunham classification) on petrophysical properties (Fig. 6).

If the area is treated as a "layer-cake" scenario, and the average permeability of each facies is considered, then there is an overall increase in permeability up section, with facies C_3, E_2, and F_2 having the highest average permeability. However, these facies are not homogeneous, and petrophysical anisotropy is common (Table 3) ($\bar{x}$Kh/Kv of whole formation = 3.4; max = 19.3, facies C_1; min = 0.2, facies D_3). The most notable examples of anisotropy are in facies B_1, C_2, D_3, and E_2 (~1–3 D).

Porosity and permeability were plotted against pore type and diagenetic process, and specifically micritization and cementation (two of the most common diagenetic processes) in Figure 7 to identify any relationships between diagenetic events and individual pore types. There are, however, no strong correlations between pore type, total porosity, and permeability. Two or more samples may have the same pore types but very different petrophysical properties; moldic, vuggy, interparticle, intercrystalline, and fracture types of porosity occur in core plugs across a range of permeabilities (<10 to >5000 mD).

Capillary pressure curves show desaturation of 16 to 80% water at <5.2 bar ($\bar{x}$ = 53%). One sample of facies B_1 had more than 90% of pore throats wider than 1-μm radius, and nearly 80% of the brine desaturated at <0.7 bar. However, the remaining pores remained saturated until the end of the experiment (Swi = 0.2; Fig. 8). In

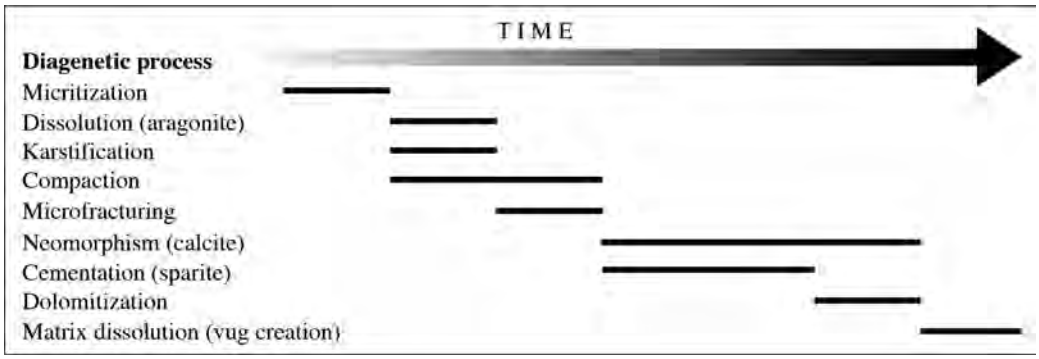

FIG. 5.—Paragenetic sequence of the Santanyí Limestone. Diagenetic phases are discussed in the text.

samples of facies C_1 and D_2, 80% of the pore throat radii are >1 μm, and <40% of the brine desaturated at <0.7 bar, with a gradual desaturation until the end of the experiment. Swi in these samples ranges from 20 to 80%. One sample of facies D_2 and a single sample of facies E_1 had the most pore-throat radii <1 μm in radius and underwent minimal desaturation at <0.7 bar. Both had Swi = initial water saturation >60% at the end of the experiment. Brine resistivity at 25° C was 0.3362 ohm, and the resistivity of the brine-saturated plugs (Ro) had a range from 11 to >200 ohm. This gives an average FRF of 1159 (32–5206).

INTERPRETATION

Depositional Environments

Main Facies: The diverse and mostly broken skeletal fragments in the coral rudstone (A) suggest reworking of reef-derived skeletal

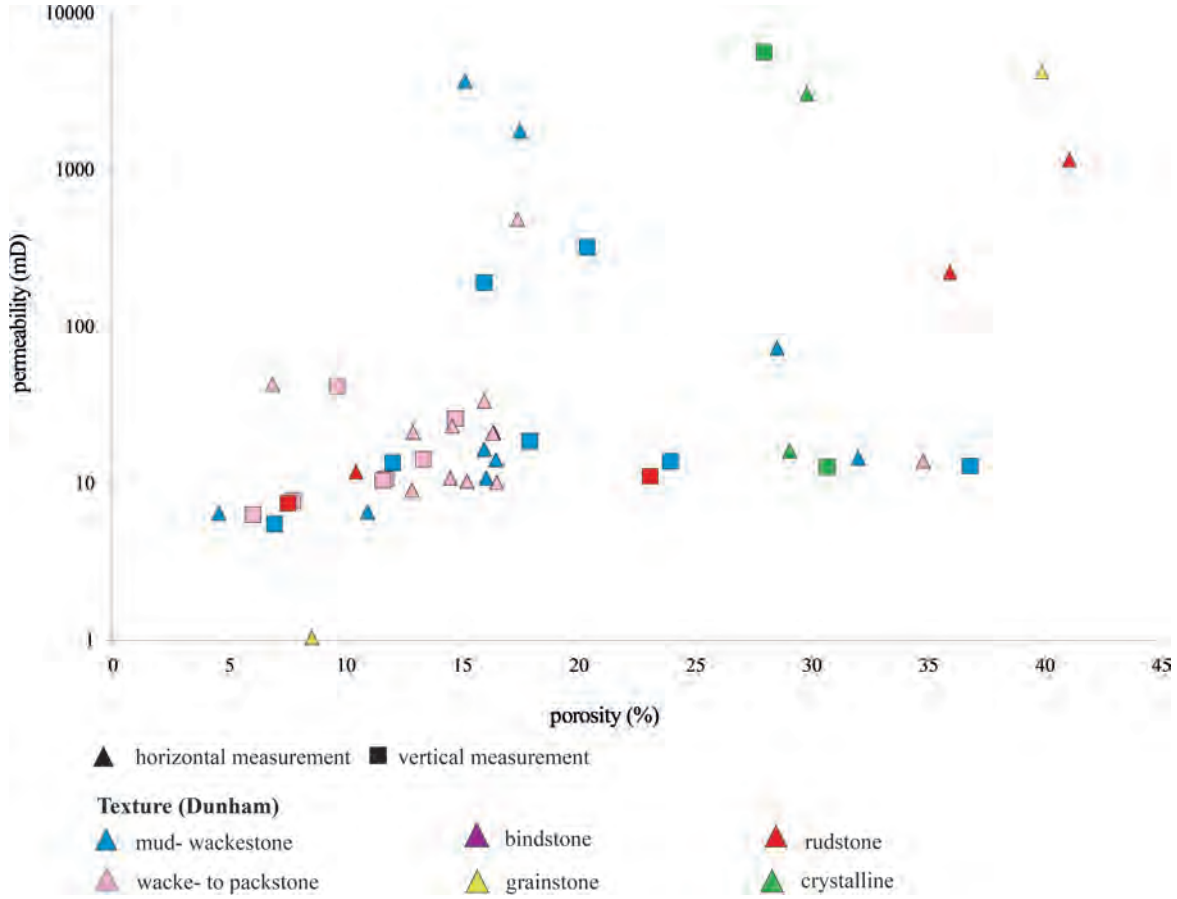

FIG. 6.—Plot of porosity vs. permeability showing variable correlation and no relation to lithofacies.

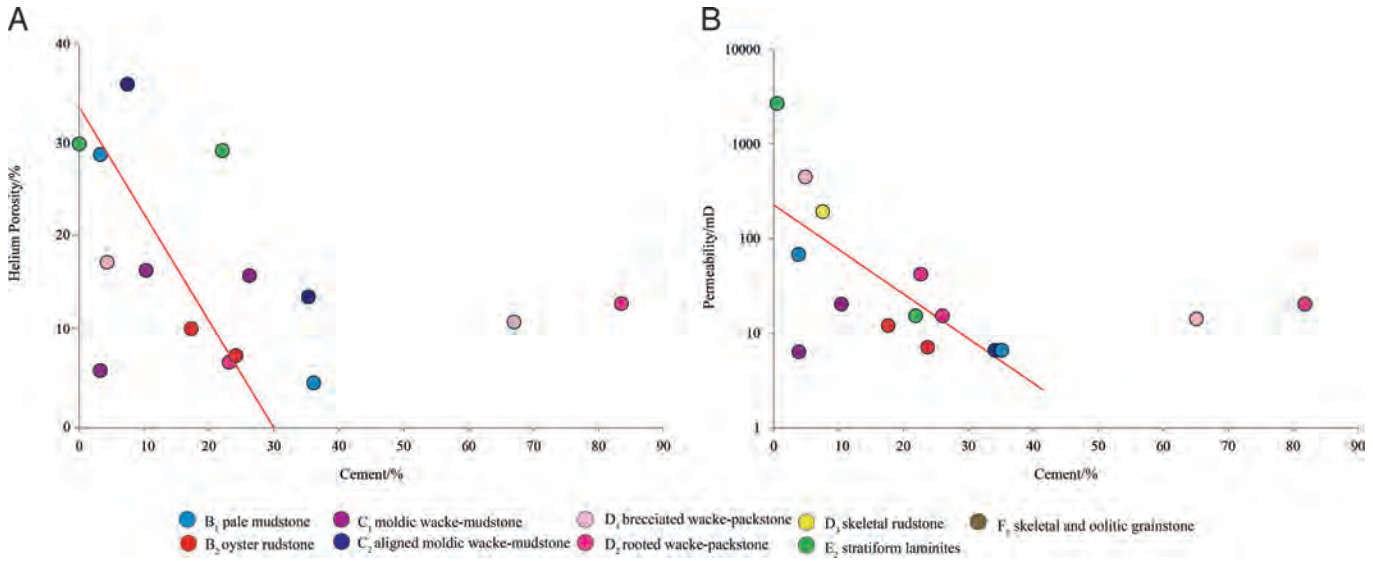

FIG. 7.—**A, B)** Plots of porosity and permeability vs. cement volume, quantified by point counting.

material by washover in a back-reef environment. The relatively lower faunal abundance and diversity in overlying mud- and skeletal wackestones (B_1, C_1, C_2), dominated by gastropods and miliolids, suggest a degree of environmental stress, although bioturbation remains common. Dasyclads are common in B_1, C_1, and C_2 and are known to populate shallow (<30 m) tropical lagoonal environments (Flügel 2004), implying subtidal protected environments, consistent with deposition of the Santanyí Limestone behind a barrier reef. Facies C_2 is interpreted to have been deposited within a lagoon, due to similarities in the matrix and pore types to B_1 and C_2, but it was affected by persistent along-shore current activity, forcing whole brachiopods and gastropods to align horizontally with the strata. Marl (H_1) is thought to represent relative sea-level fall and exposure, as evidenced by the presence of black pebbles and terrestrial minerals muscovite and montmorillonite.

Nodules and columnar pipe-like structures in wacke-packstones (D_2) strongly resemble mangrove roots forming in an intertidal environment (Shinn et al. 1969, Hardie and Ginsburg 1977, Berkeley and Rankey 2012). The association of D_2 with brecciations (D_1) suggests that roots may be controlling the degree of fragmentation. Brecciation is either organic (i.e., bioturbation by roots; Gabet et al. 2003) or related to autobrecciation in supratidal zones (Berkeley and Rankey 2012), or it is a structural feature, possibly resulting from internal karst collapse (Robledo Ardila et al. 2004). Mangroves are adapted to conditions of fluctuating salinity on tidal flats (Shinn et al. 1969, Garrett 1977). Together with the observed fecal pellets and miliolids, they indicate a low-energy, stressed environment, consistent with pond, levee, and marsh subenvironments (Shinn et al. 1969, Hardie and Ginsburg 1977, Wright 1984, Berkeley and Rankey 2012). Red micritic crusts are further indicative of subaerial exposure, with pigmentation likely caused by terrestrial muds (terra rossa) (see review in Merino and Banerjee 2008).

Stratiform laminites (E_2) colonize the intertidal and supratidal zones of tidal flats (Hardie and Ginsburg 1977). Laminations in the Santanyí Limestone are comparable to microbial smooth domal laminations of Hardie and Ginsburg (1977), although transitions to crinkly fenestral laminations exist. Smooth domal laminations occur along channel banks with limited frequency of exposure (Hardie and Ginsburg 1977). Exposure is nevertheless indicated by the red micritic crusts.

Skeletal and oolitic grainstone with cross-bedding dominates the top of the section (F_1), indicating an increase in energy level and in water depth. Currents were both unidirectional and bidirectional; they likely included tidal currents, as indicated by herringbone cross-lamination. However, tidal bundles or mud drapes were not observed. Discrete *Planolites* burrows were able to mask physical sedimentary structures (F_2) during intermittent drops in energy level. The thickness of continuous grainstones without intermittent finer deposits, dominance of current- and tide-derived sedimentary structures, and absence of channelized bed forms suggest formation as tidal bed forms in subtidal environments. These high-energy environments were host to microbial structures (G_1, G_2), and observations suggest frequent competition between physical current activity and microbial stabilizing activity (Dill 1991, Grotzinger and Knoll 1999, Paul and Peryt 2000). The occurrence and scale of microbial bioherms in the Santanyí Limestone is analogous to stromatolite bioherms found in tidal channels on the Bahamas platform (Dill 1991).

Associated Facies: Subordinate facies represent localized environments in the Santanyí Limestone. Oyster rudstones (B_2) are invariably associated with shallow subtidal (C_2) and low intertidal (D_1, D_2) facies and contain colonial corals. Oysters commonly prefer solid substrates to live, suggesting the presence of meter-scale patch reefs within the shallow subtidal lagoon zones (cf. Pomar et al. 1996). Thin-bedded packstones (E_1) lack evidence of exposure except for some micritic crusts in the upper part. *Cyclocardium* sp. bivalves live in more open lagoonal environments (Coppes 2007). Their convex-up shells indicate some degree of transport; however, currents were weak enough to leave both shells intact, differentiating their mode of formation from skeletal rudstone (D_3). On this basis, lithofacies D_3 is interpreted to have formed by winnowing/mechanical abrasion of buildups, perhaps associated with currents, leading to shell fragmentation and lack of mud.

Summary of Depositional Environments: Observations from this study are consistent with deposition of the Santanyí Limestone in a lagoonal to peritidal setting (Coppes 2007, Arenas and Pomar 2010). Temporal and spatial variations in energy level and restriction allowed a diversity of subenvironments to transition into each other. The majority of these subenvironments can be walked out laterally along

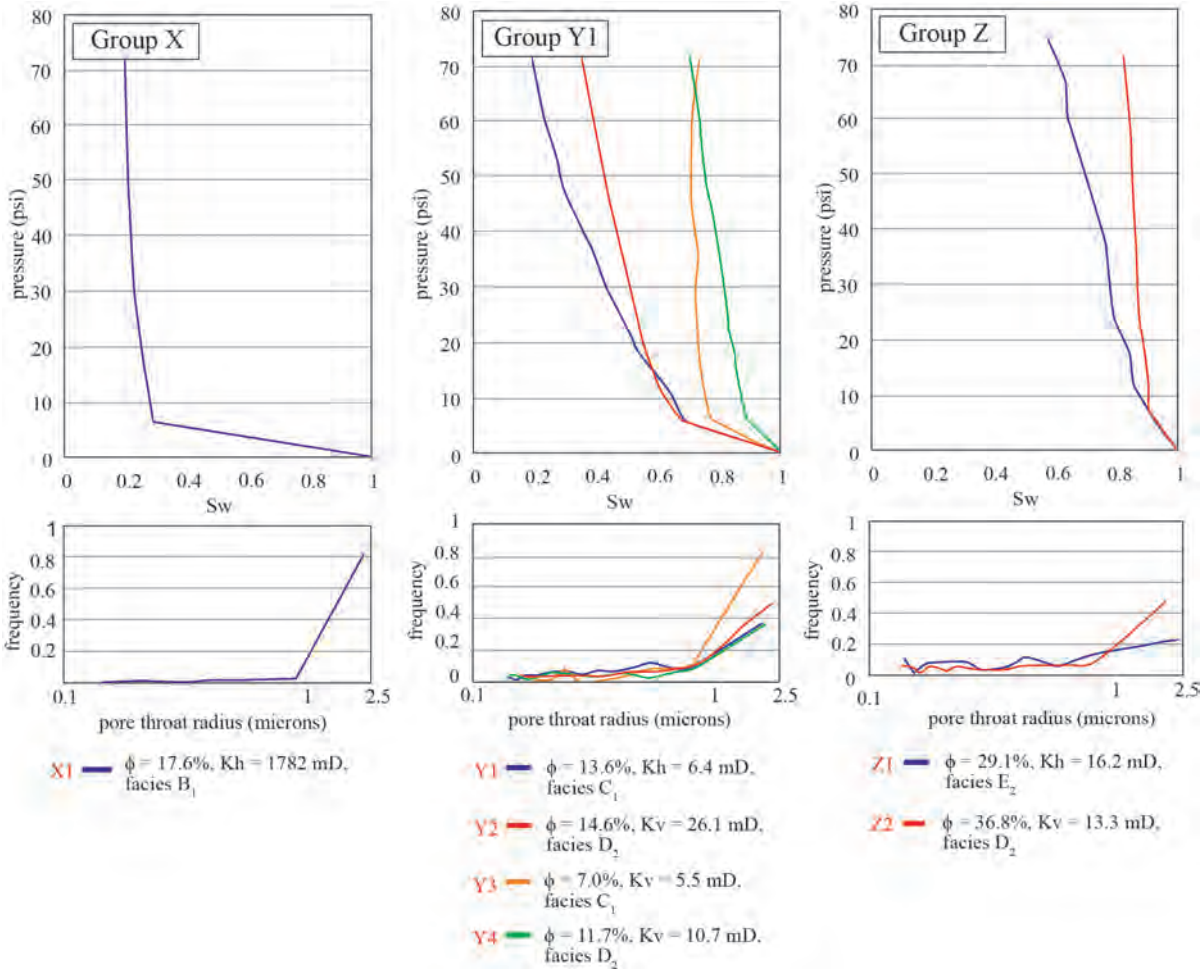

FIG. 8.—Plots of capillary pressure (P_c) and pore-throat radius frequency for samples from groups X, Y1, and Z. Group X P_c suggests a well-connected pore network. Group Y figures demonstrate high variability and a complex pore network. Group Z demonstrates very poor connectivity of pores. Note: Sw = water saturation.

strike within the 2 km study transect and form discrete layers (Fig. 3). Nevertheless, skeletal rudstone, mounded laminites, and oyster rudstones are evidence of more discrete variability and likely formed in response to the localization of currents, tidal channels, and biogenic accumulations. Thus, while the lagoonal–tidal flat facies are relatively homogeneous at a kilometer scale, facies heterogeneities develop at meter and decimeter scales. This facies patchwork is consistent with other studies of modern and ancient lagoonal environments (Shinn et al. 1969, Wright 1984, Wright and Burgess 2005).

During deposition of the Santanyí Limestone, the (now-eroded) platform margin prograded and aggraded, with deposition interrupted by emergence and erosion of the platform margin and interior (Pomar 1991). In the study area, this led to the establishment of tidal flat environments [mangroves (D_1, D_2], stratiform laminites [E_2]), followed by exposure (terra rossa crusts within E_2, and marls [H_1]). The erosional discontinuity at the top of the Santanyí Limestone records Messinian relative sea-level drop and termination of carbonate platform growth (Arenas and Pomar 2010). Depositional cyclicity is evident in the studied succession and has been interpreted previously (Pomar 1991, Pomar et al. 1996). However, it cannot confidently be interpreted based on the low thickness and extent of the study area. Moreover, the lateral and vertical heterogeneity of the formation means that it is unlikely that the formation is eustatically ordered on this scale (Wright and Burgess 2005), but could instead be controlled by autocyclic sedimentation.

Diagenetic Processes

Micritization is the earliest diagenetic phase in the Santanyí Limestone, and so it is overprinted by all subsequent diagenetic processes. Micritization occurs as a result of boring by microorganisms in shallow-marine environments (Bathurst 1975), and, in some cases, it has completely obliterated the grain fabric (D_2, D_3). The morphology of biomolds indicates that they were mostly formed by dissolution of bivalves and gastropods, which were aragonitic at deposition (Flügel 2004). The abundance of these organisms in facies B_1, C_1, and C_2 means that they are most abundant in restricted (i.e., more saline, stressed) lagoonal sediments. Recrystallization by calcite occurs within facies C_2, D_1, and D, stratiform laminites (E_2), stromatolite-containing grainstone (F_1, F_2), and, rarely, skeletal grains (F_1, D_1, D_2). The timing of this reaction is unclear from the data available for this study, but it is tentatively associated with karstification after deposition of the Santanyí Limestone, given that

the most pervasively recrystallized facies (E_1, E_2, F_1, and F_2) occur at the top of the Santanyí Limestone Formation. Recrystallization produced a fine crystal structure that destroyed the grain fabric, and that may have later undergone dissolution (E_2). Partial recrystallization (C_2, D_1, D_2) is less predictable and is not seen in outcrop but was encountered periodically in thin section.

Pore-filling cements are dominated by drusy sparry calcite, except for some uncommon isopachous cements coating grains in facies B_2 and E_2. Since most pore-filling calcite cements are sparry, drusy, and bladed and occlude primary and secondary pores, after compaction, forming between brittle fragmented and intrapenetrating grains, they are interpreted to have precipitated under shallow-burial conditions. The absence of stylolites demonstrates that the Santanyí Limestone was never buried below a few tens of meters, but a more precise timing and fluid origin cannot be determined from the current data set.

A summary study by Pomar and Ward (1999) of dolostone distribution suggested that dolomitization occurred along permeable pathways via the Reef Complex, and also along sequence boundaries. In this study area, sequence boundaries formed atop the marl facies (H_1), which is often brecciated where it is located above facies B_1 in the western part of the study area. This localized brecciation likely formed open fractures, which were conduits for fluid flow, perhaps explaining why the most intense dolomitization occurs in B_1 in this area.

Relationships among Diagenesis, Pore Types, and Petrophysical Measurements

The first phase of diagenetic modification is micritization, which can protect grains from dissolution, and which creates intraparticle microporosity. For example, grains that are completely micritized remain intact, whereas a network of micrite envelopes with a thin cement coating may be the only remnant of the original grain remaining following dissolution and/or dolomitization (black arrows, Fig. 4E). The process of micritization therefore has modified porosity by increasing micropore abundance but inhibiting moldic macropore formation. Dissolution of allochems led to abundant biomoldic porosity, but these pores appear isolated in thin section, except where there is a dense population of allochems, such as in the aligned moldic wacke-mudstone (C_1). Most likely, they are not isolated in reality; capillary pressure data indicate that most pore throats are <5 μm in diameter and therefore beneath the resolution of the petrographical microscope. Microfracturing is common and produces well-connected pore space, but the infilling of around half of all fractures by calcite cement reduces permeability.

Sparry calcite occludes macroporosity, thereby reducing porosity and permeability (Fig. 4B, C). However, even at cement volumes of $>60\%$, total porosity can remain as high as 12%, as a result of microporosity. Fabric-destructive recrystallization and dolomitization reorganized porosity to create irregular networks of intercrystalline and vuggy porosity (Fig. 4B, E).

Despite mimetic recrystallization textures in horizontally laminated facies E_2 (Fig. 4B), Kv is higher than Kh. The reasons for this are unclear but could reflect well-connected vugs and/or enhanced moldic pores. Similarly, facies D_3 shows Kv greater than Kh. There is also no unambiguous explanation for the strong anisotropy in facies B_1. At this stage, the origin of petrophysical anisotropy is difficult to predict due to its indiscriminate presence. On the other hand, facies C_3 shows strong anisotropy (Kh $>$ Kv), which can be simply attributed to the alignment of biomolds.

Microporosity varies between 0% (B_2) and 25.8% (C_1), with an average of 7.8%. Most microporosity occurs between lime mud and will also be intercrystalline in recrystallized and dolomitized lithofacies. The highest volume of macroporosity is in facies D_1 (41.1%), more than double the average value of 18.0%. Perhaps this is a result of deposition in a swampy, muddy environment with abundant large bioclasts leading to skeletal macropores. A total lack of microporosity in B_2 is unexpected due to the high volume of micrite; however, large shell biomolds in thin section likely misrepresent the volume of microporosity.

Capillary pressure curves show that the most efficient drainage occurs in the sample with the widest pore throats, as would be expected. This particular sample (CF5; facies B_1) was deposited as a skeletal mud- to wackestone, but it has undergone fabric-destructive dolomitization to form a well-connected intercrystalline pore network. In comparison, less efficient desaturation occurs in coarser and muddier samples (facies C_1 [TN2v] and D_2 [TN4v]), which have abundant moldic pores that are unconnected or connected by narrow pore throats. In these samples, the broad range of desaturation curves is consistent with pore and pore-throat heterogeneity. Despite higher permeability than in samples with moderately efficient desaturation curves, the two samples with the lowest desaturation (highest Swi) have narrower pore throats. Overall, the range of resistivity (Ro) and FRF reflects a high degree of pore network complexity.

DISCUSSION

Postdepositional Evolution of Porosity

Depositional setting and energy will control the primary porosity of a sediment by influencing grain type, grain size, and sorting. Since there is wide variation in depositional energy and water depth within nearshore subtidal and peritidal environments, there is likely significant variability in the initial porosity and permeability of the sediment. For example, primary intergranular porosity would have been high in oolitic grainstones, while stratiform laminites and skeletal mudstones and wackestones would have had high volumes of microporosity and lower permeability. Modern aragonitic muds can have depositional porosity up to 61 to 78% (Anselmetti and Eberli 1993).

These primary variations in rock properties will influence the diagenetic susceptibility of a facies. Since oolitic grainstones have a well-connected pore network at deposition, they will most likely control the flux of diagenetic fluids, leading to porosity destruction in many cases by calcite cementation. Conversely, some of the highest porosity and permeability values are measured in pale mudstone, which would have had high depositional volumes of microporosity, and hence low permeability, but which have been dolomitized, enlarging pore sizes and increasing the effective porosity. Furthermore, biomoldic porosity is developed most commonly in samples with a high abundance of aragonitic grains; this relationship was also noted by Pomar and Ward (1999).

Overall, the highest permeability was measured where densely packed bivalve and gastropod molds were horizontally aligned, and hence the initial density of packing and alignment of grains controlled the porosity and permeability of moldic wacke-mudstone (C_2). Similarly, in coquinas (D_3), densely packed skeletal grains and a lack of micrite or cement provided a highly porous, well-connected pore network. However, this facies is rare and resulted from localized depositional processes, thus limiting its potential to form a laterally correlatable flow unit. In summary, the diagenetic pathway followed by each facies after deposition was in many cases far more important to controlling its pore system than its primary depositional rock properties.

Controls on Diagenetic Pathway

The results of this study show no correlations among pore type, total porosity, and permeability. However, when combined diagenetic

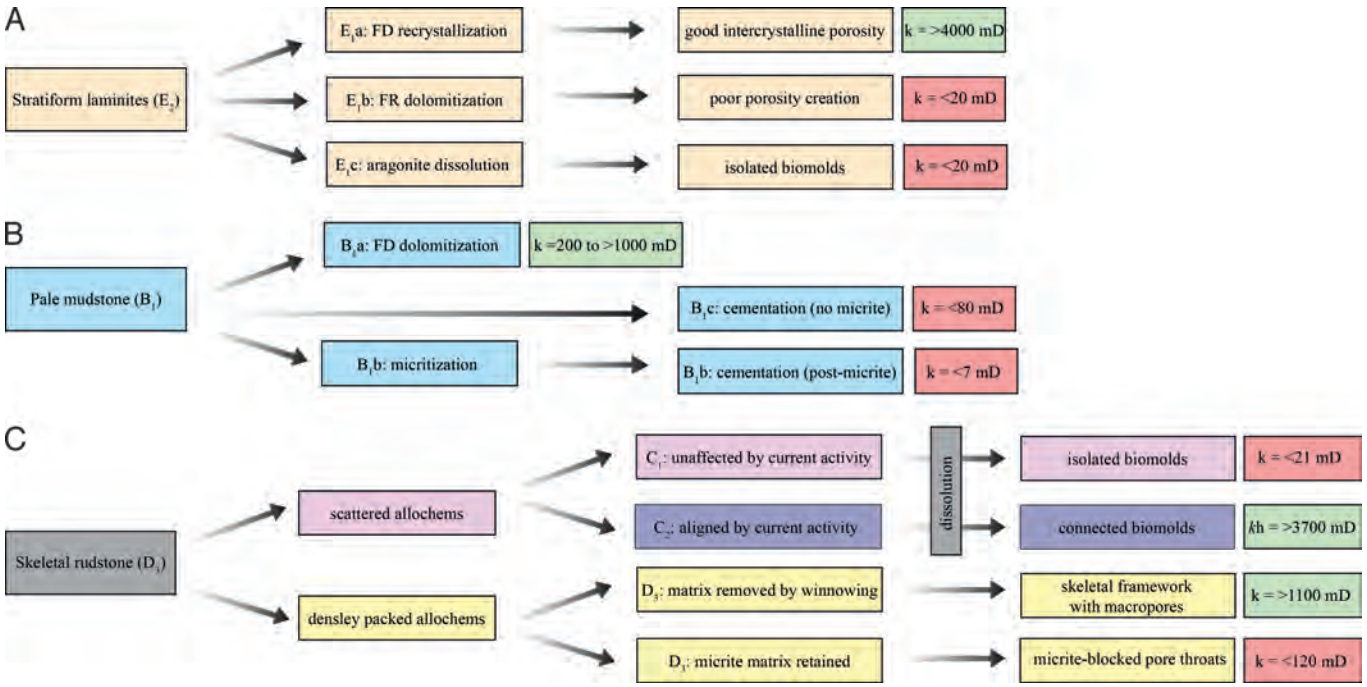

FIG. 9.—**A, B)** Potential diagenetic and **C)** sedimentological pathways for the best potential flow units identified in the study.

processes are linked to pore type, stronger trends emerge. In particular, core plugs with the highest permeability are dolomitized (B_1), recrystallized (fabric destructive; E_2, F_1), or microfractured (C_2), or they possess a high density of aligned biomolds (C_2). Samples with the lowest permeability are micritized and cemented and have isolated biomolds. There is a moderate inverse correlation between the volume of cement and porosity (Fig. 7A; $R^2 = 0.5$), which decreases sharply with increasing cement volumes up to 35%; at higher cement volumes, total porosity appears unchanged, principally reflecting the volume of microporosity. This observation is limited to two samples with cement volumes >35%; however ,a similar trend is seen for permeability (Fig. 7b; $R^2 = 0.7$). There is no overall correlation among porosity, permeability, and micrite ($R^2 = <0.04$). However, the highest permeability is associated with 0% micrite, reflecting an absence of primary micrite or micrite-destructive recrystallization (E_2). A high micrite content but high permeability is associated with grain micritization but a lack of sediment matrix (D_1, D_3).

Nevertheless, a single diagenetic process cannot be linked to specific petrophysical properties. For example, fabric-destructive recrystallization and dolomitization only create a well-connected pore network in some samples (Kh <1 mD to >500 mD). Similarly, dissolution of aragonitic allochems to form biomoldic porosity results in a wide range of permeability (Kh = <10 mD to >1D; Fig. 7A).

Figure 9 maps the potential diagenetic pathways of an individual lithofacies after deposition, based on petrographical observation. From this, certain trends emerge (Fig. 9A–C).

- Dolomitization is focused within fine-grained mudstones and stratiform laminites. This might reflect the higher reactive surface area of these facies (Al-Helal et al. 2012), proximity to the dolomitizing brine pool, or an initiation of dolomitization by microbial process via very high magnesium dolomite (e.g., see discussion in Gregg et al. 2015). If, however, these facies were only partially dolomitized, or recrystallization was fabric retentive, then permeability remained low.
- Recrystallization appears to have taken place primarily beneath the top Santanyí Limestone and might have been related to karstification and ingress of meteoric water (e.g., Budd 1989). It created a well-connected intercrystalline pore network, which was further enhanced by the formation of vugs—perhaps also during karstification—creating a highly permeable pore network.
- Biomoldic porosity can form a highly effective pore system (Kh >3D) when precursor grains were densely packed and aligned, as a connected pore system was created, but dissolution of isolated grains did not improve permeability, and Kh is <20 mD.

In other words, the diagenetic pathway that a particular facies follows is related to both its original texture and its position in the depositional succession, which dictates the fluids that will modify its rock properties (e.g., through dolomitization or recrystallization).

Integration of Petrophysics, Diagenesis, and Facies

Using the pore evolution pathways presented in Figure 9, it is possible to separate the petrophysical database into three groups (X, Y, Z; Fig. 10; Table 4).

Core plugs in group X have high permeability (39.0–5677 mD, $\bar{x}$ = 1316 mD) and moderate to good porosity (6.9–36%, $\bar{x}$ = 20.2%) (Fig. 10), with a well-connected pore network and multiple pore types: moldic (94% of samples), vuggy (70%), intercrystalline (47%), fracture (24%), and interparticle (12%). The samples with highest permeability have experienced fabric-destructive matrix recrystallization (E_2) and fabric-destructive (FD) dolomitization (B_1) (Fig. 4A, E). The resultant simple pore network facilitates high flow rates, evidenced by the capillary pressure (P_c) curve, which suggests a well-connected pore network with desaturation of 80% water at <5.2 bar (Fig. 8). The lowest FRF (<100), which represents the simplest pore system, occurs in this petrophysical group with Ro <100 ohm, indicative of a conductive fluid path via brine-filled pores. Pore throats

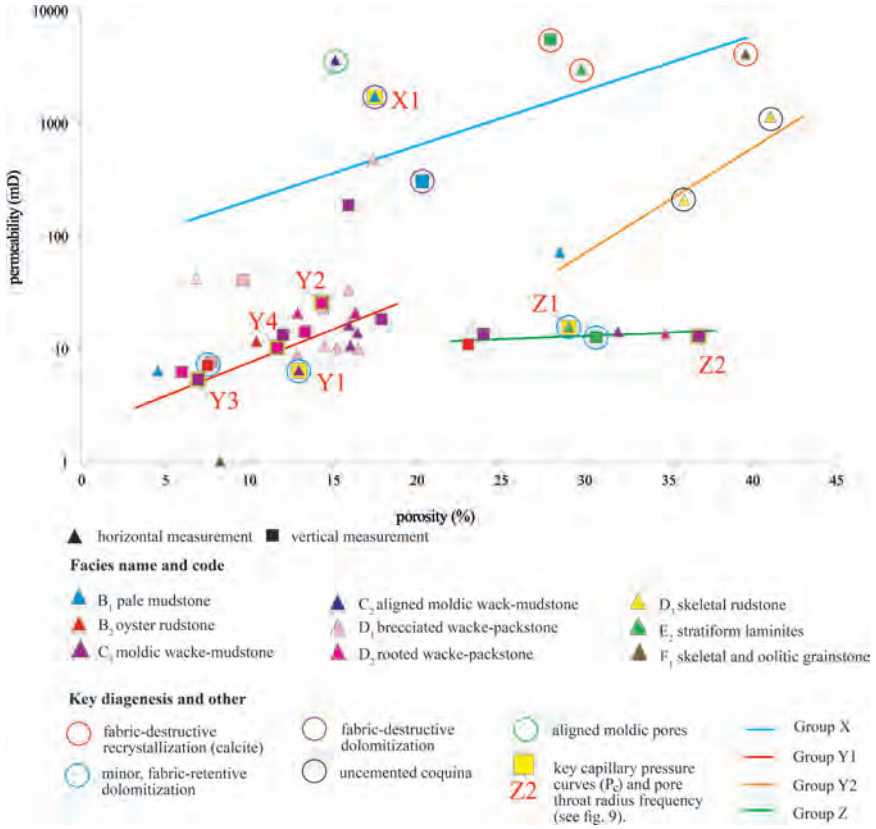

FIG. 10.—Plot of porosity vs. permeability with interpretations. The positive correlation between porosity and permeability can be approximately subdivided into three groups: X, Y, and Z. From this, it is clear that a relationship between porosity and permeability is not driven by facies, but by diagenesis.

are typically wide (>1 μm), and micropore volumes are low ($\bar{x}$ = 7.9%).

In group Y, core plugs have moderate permeability (65–1166 mD, $\bar{x}$ = 193 mD), and variable porosity (4.6–41.1%, $\bar{x}$ = 14.6%) (Fig. 10). Group Y represents samples with the most complex pore networks, indicated by a FRF of >700 (up to >>1000), and it has been subdivided into Y1 and Y2 to represent this. Group Y1 core plugs are micrite rich (B_2, C_1, D_1, D_2) and have consistently low to moderate permeability of <100 mD. This group includes samples with a range of pore sizes and pore types that are moderately well connected. At the same time, samples have the most complex pore evolution, including partial fabric-retentive dolomitization (Fig. 4F), and grain dissolution (moldic porosity in 75% of samples, connected vugs in 50% of samples, although often cemented; Fig. 4C). Capillary pressure curves suggest a moderately well-connected pore network, with desaturation of up to 65% water at <5.2 bar (Fig. 8). Higher permeability was measured in group Y2, dominated by skeletal rudstone facies (D_3), which lack cement and have well-connected porosity (ϕ = 15.1%, k = 3271 mD) (Fig. 10). Vugs are present in all samples in group Y, adding to pore-scale complexity. Importantly, it is merely a coincidence that groups Y1 and Y2 fit the same porosity-permeability trend, because they possess different pore evolution pathways and different pore networks. In a hydrocarbon reservoir, therefore, they are highly likely to have very different relative permeability and recovery efficiency (see discussion in Hollis et al. 2010).

TABLE 4.—R^2 values of groups defined by diagenetic pathway.

Group	n	R^2
X	11	0.4
Y1	24	0.4
Y2	8	0.8
Z	8	0.1

Group Z comprises core plugs that have invariant, poor permeability (~10 mD) for a range of porosity (23.1–36.8%, $\bar{x}$ = 30.1%) (Fig. 10). These samples possess >10% micrite, >15% cement, or high volumes of microporosity (up to 36.8%; Fig. 4A, D). Partial, fabric-retentive dolomitization has occurred in some samples in group Z, but this does not improve permeability. The P_c curve (Fig. 8) indicates very poor connectivity of pores (only 16% of water desaturated at 4.9 bar), while a very low resistivity (11 ohm) and very low FRF are suggestive of a very simple, well-connected pore network, most likely facilitated by connected microporosity.

CONCLUSIONS AND IMPLICATIONS

This research highlights the complexities of characterizing petrophysical properties in shallow-marine carbonate environments.

- The Santanyí Limestone Formation represents a Miocene-age shallow subtidal and peritidal environment consisting of six main facies and six subordinate facies.

- The paragenetic sequence was determined to be micritization, aragonite dissolution, karstification, fracturing, compaction, recrystallization, cementation, sparite dissolution, and dolomitization (partial and fabric-destructive types).
- Porosity and permeability show no singular correlation to facies or a unique diagenetic process; rather, diagenetic modification was influenced by both lithofacies and its position in the sedimentary sequence.
- The integration of sedimentary, diagenetic, and petrophysical data is essential to classify pore networks and group them into potential flow units.

ACKNOWLEDGMENTS

The authors would like to express their great appreciation to Luis Pomar of Universitat de Les Illes Balears for his fundamental research of the Miocene of Mallorca and his support throughout this project. They would also like to extend their thanks to Steven Stockley and Ray Leadbitter for preparation of thin sections and to Steven May for his support with the petrophysical laboratory equipment at the University of Manchester. The authors would like to thank Alex MacNeil and volume editor Don McNeill for insightful comments that significantly improved the quality of this manuscript

REFERENCES

Adam A, Swennen R, Abdulghani W, Abdlmutalib A, Hariri M, Abdulraheem A. 2018. Reservoir heterogeneity and quality of Khuff carbonates in outcrops of central Saudi Arabia. *Marine and Petroleum Geology* 89:721–751.

Ahr WM. 2008. *Geology of Carbonate Reservoirs: The Identification, Description and Characterization of Hydrocarbon Reservoirs in Carbonate Rocks*: Wiley & Sons, Hoboken, New Jersey. 296 p.

Al-Helal A, Whitaker F, Xiao Y. 2012. Reactive transport modelling of brine reflux: Dolomitization, anhydrite precipitation and porosity evolution. *Journal of Sedimentary Research* 82:196–215.

Alvaro M, Barnolas A, Del Olmo P, Ramirez del Pozo J, Simo A. 1984. Sedimentología del Jurásico de Mallorca. *In* Barnolas-Cortinas A (Editor). *Libro Guía de la Excursión, Grupo Espanyol del Mesozoico, Palma de Mallorca*: Instituto Geológico y Minero de España, Madrid. 263 p.

Anselmetti FS, Eberli GP. 1993. Controls on sonic velocity in carbonates. *Pure and Applied Geophysics* 141:287–323.

Arenas C, Pomar L. 2010. Microbial deposits in Upper Miocene carbonates, Mallorca, Spain. *Palaeogeography, Palaeoclimatology, Palaeoecology* 297:465–485.

Bathurst RGC. 1975. *Carbonate Sediments and Their Diagenesis*: Elsevier, Amsterdam. 658 p.

Berkeley A, Rankey EC. 2012. Progradational Holocene carbonate tidal flats of Crooked Island, south-east Bahamas: An alternative to the humid channeled belt model. *Sedimentology* 59:1902–1925.

Bernoulli D, Jenkyns HC. 1974. Alpine, Mediterranean and central Atlantic Mesozoic facies in relation to the early evolution of the Tethys. *In* Dott RH, Shaver RH (Editors). *Modern and Ancient Geosynclinal Sedimentation*, Special Publication 19: SEPM (Society for Sedimentary Geology), Tulsa, Oklahoma. p. 129–160.

Bizon G, Bizon J-J, Biju-Duval B. 1978. Comparison between formations drilled at DSDP Site 372 in the western Mediterranean and exposed series on land. *Initial Reports of DSDP* 42:897–901.

Budd D. 1989. Microrhombic calcite and microporosity in limestones: A geochemical study of the Lower Cretaceous Thamama Group, UAE. *Sedimentary Geology* 62:293–311.

Choquette PW, Pray LC. 1970. Geological nomenclature and classification of porosity in sedimentary carbonates. *American Association of Petroleum Geologists Bulletin* 54:207–250.

Coppes H. 2007. An integrated study into the reservoir characteristics of Miocene mangrove deposits of Mallorca [unpublished MSc Thesis]: Technische Universiteit Delft, Netherlands. 226 p.

Dill RF. 1991. Subtidal stromatolites, ooids and crusted-lime muds at Great Bahama Bank margin. *In* Osborne RH (Editor). *From Shoreline to Abyss*, Special Publication 46: SEPM (Society for Sedimentary Geology), Tulsa, Oklahoma. p. 147–171.

Flügel E. 2004. *Microfacies of Carbonate Rocks*: Springer, Heidelberg, Germany. 976 p.

Fournier F, Montaggioni L, Borgomano J. 2004. Paleoenvironments and high-frequency cyclicity from Cenozoic South-East Asian shallow-water carbonates: A case study from the Oligo-Miocene buildups of Malampaya (offshore Palawan, Philippines). *Marine and Petroleum Geology* 21:1–21.

Gabet EJ, Reichman OJ, Seabloom EW. 2003. The effects of bioturbation on soil process and sediment transport. *Annual Review of Earth and Planetary Sciences* 31:249–273.

Garrett P. 1977. Biological communities and their sedimentary record. *In* Hardie LA (Editor). *Sedimentation on the Modern Carbonate Tidal Flats of Northwest Andros Islands; Bahamas*, The Johns Hopkins University Studies in Geology 22: The John Hopkins University Press, Baltimore, Maryland. p. 124–158.

Gelabert B, Sabat F, Rodriguez-Perea A. 1992. A structural outline of the Serra de Tramuntana of Mallorca (Balearic Islands). *Tectonophysics* 203:167–183.

Gregg J, Bish D, Kaczmarek S, Machel H. 2015. Mineralogy, nucleation and growth of dolomite in the laboratory and sedimentary environment: A review. *Sedimentology* 62:1749–1769.

Grélaud C, Razin P, Homewood P. 2010. Channelized systems in an inner carbonate platform setting: Differentiation between incisions and tidal channels (Natih Formation, Late Cretaceous, Oman). *In* van Buchem FSP, Gerdes KD, Esteban M (Editors). *Mesozoic and Cenozoic Carbonate Systems of the Mediterranean and the Middle East: Stratigraphic and Diagenetic Reference Models*, Special Publications 329: Geological Society, London. p. 163–186.

Grotzinger JP, Knoll AH. 1999. Stromatolites in Precambrian carbonates: Evolutionary mileposts or environmental dipsticks? *Annual Review of Earth and Planetary Sciences* 27:313–358.

Hardie LA, Ginsburg RN. 1977. Layering: The origin and environmental significance of lamination and thin bedding. *In* Hardie LA (Editor). *Sedimentation on the Modern Carbonate Tidal Flats of Northwest Andros Islands; Bahamas*, The Johns Hopkins University Studies in Geology 22: The John Hopkins University Press, Baltimore, Maryland. p. 50–123.

Hollis C. 2011. Diagenetic controls on reservoir properties of carbonate successions within the Albian–Turonian of the Arabian Plate. *Petroleum Geoscience* 17:223–241.

Hollis C, Lawrence DA, Deville de Perière M, Al Darmaki F. 2017. Controls on porosity preservation within a Jurassic oolitic reservoir complex, UAE. *Marine and Petroleum Geology* 88:888–906.

Hollis C, Vahrenkamp VC, Tull S, Mookerjee A, Taberner C, Huang Y. 2010. Pore system characterization in heterogeneous carbonates: An alternative approach to widely-used rock-typing methodologies. *Marine and Petroleum Geology* 27:772–793.

James N. 1984. *Origin of Carbonate Sedimentary Rocks*: John Wiley & Sons, Chichester, West Sussex, UK. 464 p.

Lucia JF. 2007. *Carbonate Reservoir Characterization, An Integrated Approach*: Springer, Berlin. 336 p.

Marchionda E, Deschamps R, Cobianchi M, Nader F, Di Giulio A, Morad D, Al Darmaki F, Ceriant A. 2018. Field-scale depositional evolution of the Upper Jurassic Arab Formation (onshore Abu Dhabi, UAE). *Marine and Petroleum Geology* 89:350–369.

Merino E, Banerjee A. 2008. Terra Rossa genesis, implications for karst, and eolian dust: A geodynamic thread. *The Journal of Geology* 116:62–75.

Morrow DW. 1982. Descriptive field classification of sedimentary and diagenetic breccia fabrics in carbonate rocks. *Bulletin of Canadian Petroleum Geology* 30:227–229.

Paul J, Peryt TM. 2000. Kalkowsky's stromatolites revisited (Lower Triassic Buntsandstein, Harz Mountains, Germany). *Palaeogeography, Palaeoclimatology, Palaeoecology* 161:435–458.

Pomar L. 1991. Reef geometries, erosion surfaces and high-frequency sea-level changes, Upper Miocene Reef Complex, Mallorca, Spain. *Sedimentology* 38:243–269.

Pomar L, Ward WC. 1999. Reservoir-scale heterogeneity in depositional packages and diagenetic patterns on a reef-rimmed platform, Upper Miocene, Mallorca, Spain. *American Association of Petroleum Geologists Bulletin* 83:1759–1773.

Pomar L, Ward WC, Green DG. 1996. Upper Miocene reef complex of the Llucmajor area, Mallorca, Spain. *In* Franseen EK, Esteban M, Ward WC, Rouchy J-M (Editors). *Models for Carbonate Stratigraphy from Miocene Reef Complexes of Mediterranean Regions*, Concepts in Sedimentology and Paleontology 5: SEPM (Society for Sedimentary Geology), Tulsa, Oklahoma. p. 191–225.

Robledo Ardila PA, Durán JJ, Pomar L. 2004. Paleocollapse structures as geological record for reconstruction of past karst processes during the Upper Miocene of Mallorca island. *International Journal of Speleology* 33:81–95.

Sàbat F, Gelabert B, Rodriguez-Perea Giménez J. 2011. Geological structure and evolution of Majorca: Implications for the origin of the Western Mediterranean. *Tectonophysics* 510:217–238.

Shinn EA, Lloyd RM, Ginsburg RN. 1969. Anatomy of modern carbonate tidal-flat, Andros Island, Bahamas. *Journal of Sedimentary Petrology* 39:1202–1228.

Skalinski M, Kenter J. 2015. Carbonate petrophysical rock typing: Integrating geological attributes and petrophysical properties while linking with dynamic behavior. *In* Agar SM, Geiger S (Editors). *Fundamental Controls on Fluid Flow in Carbonates: Current Workflows to Emerging Technologies*, Special Publication 406: Geological Society, London. p. 229–259.

Strohmenger CJ, Ghani A, Al-Jeelani O, Al-Mansoori A, Al-Dayyani T, Weber LJ, Al-Mehsin K, Vaughan L, Khan SA, Mitchell JC. 2006. High-resolution sequence stratigraphy and reservoir characterization of Upper Thamama (Lower Cretaceous) reservoirs of a giant Abu Dhabi oil field, United Arab Emirates. *In* Harris PM, Weber LJ (Editors). *Giant Hydrocarbon Reservoirs of the World: From Rocks to Reservoir Characterization and Modeling*, Memoir 88: American Association of Petroleum Geologists, Tulsa, Oklahoma. p. 139–171.

van Buchem FSP, Pittet H, Hillgärtner H, Grötsch J, Al Mansouri AI, Billing IM, Oterdoom WH, van Steenwinkel M. 2002. High-resolution sequence stratigraphic architecture of Baremian/Aptian carbonate systems in northern Oman and the United Arab Emirates (Kharaib and Shuaiba formations). *GeoArabia* 7:461–500.

Wright VP. 1984. Peritidal carbonate facies models: A review. *Geological Journal* 19:309–325.

Wright VP, Burgess PM. 2005. The carbonate factory continuum, facies mosaics and microfacies: An appraisal of some of the key concepts underpinning carbonate sedimentology. *Facies* 51:17–23.